Accurate modeling of the dynamics of dissociative chemisorption on metal surfaces

Gerrits, N.

Chapter 2

Methods and Theory

In this chapter, the theoretical framework for the electronic structure calculations and molecular dynamics (MD) for molecule-metal surface reactions is introduced. Section 2.1 concerns the electronic structure calculations, for which density functional theory (DFT) is employed. Section 2.2 discusses how the MD is performed. In Section 2.3 two different methods for fitting potential energy surfaces (PESs) are briefly discussed. Finally, Section 2.4 explains how the initial conditions for MD simulations are generated and Section 2.5 shows how observables can be computed from the MD simulations.

2.1 Density Functional Theory

In theoretical chemistry, typically the Born-Oppenheimer approximation (BOA) is used, which separates the motion of nuclei and electrons[1]. From the BOA follows that the most important and difficult property to be addressed by MD simulations is the electronic structure. The most popular method in calculating the electronic structure is DFT. Its success lies in its relatively low computational cost and favorable scaling with system size, combined with its accuracy. The basis of DFT relies on the fact that the ground state wave function is uniquely defined by the electron density, which has been proposed by Hohenberg and Kohn[2]. Hereafter, Kohn and Sham proposed a strategy in actually obtaining the ground state electronic density and concomitant wave function[3]. Their strategy involved introducing a fictitious system of non-interacting electrons and solving the one-electron Kohn-Sham (KS) equations:

$$\left[-\frac{1}{2}\nabla^2 + V_\mathrm{s}(\mathbf{r})\right]\psi_i(\mathbf{r}) = \epsilon_i\psi_i(\mathbf{r}), \tag{2.1}$$

where the first term is the kinetic energy operator, V_s is the effective potential, $\psi_i(\mathbf{r})$ is the KS wave function at $\mathbf{r} = (x, y, z)$, and ϵ_i is the KS orbital energy.

Note that all equations in this section are given in Hartree atomic units, i.e., $\hbar = e = m_e = 1$. From the KS orbitals the electron density ρ can be constructed:

$$\rho(\mathbf{r}) = \sum_i |\psi_i(\mathbf{r})|^2. \tag{2.2}$$

Furthermore, the effective potential is defined as

$$V_s(\mathbf{r}) = \int \frac{\rho(\mathbf{r}')}{|\mathbf{r} - \mathbf{r}'|} \, d\mathbf{r}' - \sum_N \frac{Z_N}{|\mathbf{r} - \mathbf{R}_N|} + V_{XC}(\mathbf{r}), \tag{2.3}$$

where Z_N and $\mathbf{R}_N$ are the charges and positions of the nuclei, respectively. The first term is the electron-electron repulsion, the second term is the electron-nuclei attraction, and the final term is the exchange-correlation (XC) potential, which contains all non-classical interaction energy terms and is the derivative of the XC-energy with respect to the electron density as follows:

$$V_{XC}(\mathbf{r}) = \frac{\delta E_{XC}(\mathbf{r})}{\delta \rho(\mathbf{r})}. \tag{2.4}$$

Although DFT is in principle exact, the exact functional form of the exchange-correlation potential is unknown and is at present still improved upon in order to increase the accuracy of DFT. Different functional forms and approximations will be discussed in the next Section.

2.1.1 Exchange-Correlation Functionals

Unfortunately, the exact expression for the exchange-correlation (XC) density functional (DF) is unknown, requiring approximations to the exact XC-DF. It is tempting to refer to the so-called Jacob's ladder[4] when discussing the many available approximations to the exact XC-DF. This ladder attempts to systematically rank the approximations and their "ingredients" in terms of accuracy (and coincidentally of computational cost). For instance, the first rung only relies on the local electron density, whereas the second and third rungs add the first and second derivatives of the electron density, respectively. Regrettably, Jacob's ladder contains several inconsistencies. For example, Perdew and Schmidt stated that in the design of Jacob's ladder ingredients of lower rungs cannot be removed when climbing the ladder[4]. However, the fourth rung includes, among others, the hybrid generalized gradient approximation (GGA), which does not make use of the Laplacian employed in the meta-GGA (MGGA) belonging to the third rung. Furthermore, neither the dispersion corrected nor the vdW non-local correlation DFs currently

have a place on the ladder, and it is unclear where they should be positioned since they also do not belong to the fifth rung of the non-local exact partial correlation methods. Some attempts have been made to improve Jacob's ladder (e.g., by introducing rungs between the existing rungs), but it remains rather inconsistent. Therefore, in the discussion of several approximations to the XC-DF, here, I will refrain from employing a "ranking" such as Jacob's ladder and merely try to categorize the approximations.

Local Density Approximation

The most simple approximation is the local density approximation (LDA), where the electrons are assumed to behave as a homogeneous electron gas (or jellium). The XC energy $E_{\mathrm{XC}}^{\mathrm{LDA}}$ only depends on the local electron density $\rho(\mathbf{r})$ and can be written as

$$E_{\mathrm{XC}}^{\mathrm{LDA}}(\rho(\mathbf{r})) = \int \rho(\mathbf{r}) \left[\epsilon_{\mathrm{X}}(\rho(\mathbf{r})) + \epsilon_{\mathrm{C}}(\rho(\mathbf{r}))\right] \mathrm{d}\mathbf{r}, \tag{2.5}$$

where ϵ_{X} and ϵ_{C} are the exchange and correlation energies per electron, respectively. The exchange energy in a jellium can be analytically computed as[5]

$$\epsilon_{\mathrm{X}}(\rho(\mathbf{r})) = -\frac{3}{4}\left(\frac{3}{\pi}\rho(\mathbf{r})\right)^{\frac{1}{3}}. \tag{2.6}$$

However, for the correlation energy in a jellium, exact analytical expressions only exist for the low- and high-density limits. Therefore, analytical correlation DFs are either fitted to accurate quantum Monte Carlo results for a jellium[6–9] or derived from physical constraints[10].

Generalized Gradient Approximation

The LDA can be extended by including the gradient of the local electron density as well, being the so-called GGA:

$$E_{\mathrm{XC}}^{\mathrm{GGA}}\left(\rho(\mathbf{r}), \nabla\rho(\mathbf{r})\right) = \int f\left[\rho(\mathbf{r}), \nabla\rho(\mathbf{r})\right] \mathrm{d}\mathbf{r}, \tag{2.7}$$

which subsequently can be separated into a separate exchange ($E_{\mathrm{X}}^{\mathrm{GGA}}$) and correlation ($E_{\mathrm{C}}^{\mathrm{GGA}}$) energy (as is done for the LDA). Note that a non-separable gradient approximation also exists, which is similar to the GGA but where the exchange and correlation are non-separable[11, 12]. The exchange part is

defined as

$$E_{\mathrm{X}}^{\mathrm{GGA}}\left(\rho(\mathbf{r}), \nabla\rho(\mathbf{r})\right) = \int \rho(\mathbf{r})\epsilon_{\mathrm{X}}(\rho(\mathbf{r}))F(s)\,\mathrm{d}\mathbf{r}, \tag{2.8}$$

where $F(s)$ is the enhancement factor and s is the dimensionless reduced density gradient:

$$s = \frac{|\nabla\rho|}{2(3\pi^2)^{1/3}\rho(\mathbf{r})^{4/3}}. \tag{2.9}$$

In the Perdew, Burke and Ernzerhof (PBE) GGA DF[13] the enhancement factor is defined as

$$F^{\mathrm{PBE}}(s) = 1 + \kappa\left(1 - \frac{1}{1 + \mu s^2/\kappa}\right), \tag{2.10}$$

where $\kappa = 0.804$ and $\mu = \beta(\pi^2/3) \simeq 0.21951$, which are constants derived from physical constraints[13]. Furthermore, for the revised PBE (RPBE) DF[14] the enhancement factor is defined in a slightly different manner than for the PBE DF, while keeping the κ and μ constants from the PBE DF, in an effort to improve chemisorption energies without violating the Lieb-Oxford bound[15–17]:

$$F^{\mathrm{RPBE}}(s) = 1 + \kappa\left(1 - e^{-\mu s^2/\kappa}\right). \tag{2.11}$$

This change in the functional form of the enhancement factor is also the reason why the PBE DF is more attractive, i.e., yields lower molecule-metal surface interaction energies, than the RPBE DF as both DFs use the same correlation DF[14]. The GGA correlation DF is typically expressed as

$$E_{\mathrm{C}}^{\mathrm{GGA}}\left(\rho(\mathbf{r}), \nabla\rho(\mathbf{r})\right) = \int \rho(\mathbf{r})\left[\epsilon_{\mathrm{C}}(\rho(\mathbf{r})) + H\left(\rho(\mathbf{r}), \nabla\rho(\mathbf{r})\right)\right]\,\mathrm{d}\mathbf{r}, \tag{2.12}$$

where H is the gradient contribution, which is specific to the DF used.

Meta-Generalized Gradient Approximation

The next obvious extension to make to the approximation of the exact XC-DF is to include the second derivative of the electron density (i.e., the Laplacian), resulting in the MGGA DFs. The inclusion of the Laplacian solves the issue of GGA DFs not being able to satisfy all the theoretical constraints on the exact functional, which is also the reason why GGA DFs tend to be good for either molecules or solids, but never for both[12, 18]. However, for numerical reasons, typically the kinetic energy density $\tau(\mathbf{r})$ for the occupied KS orbitals (i.e., the Laplacian of the KS orbitals) is used instead of the Laplacian of

the electron density[12, 19]. Nevertheless, the two are related since the KS orbitals are non-local functionals of the electron density and can therefore be interchanged in the design of an MGGA DF[20]. Similar to the LDA and GGA XC energy, the MGGA XC energy is expressed as

$$E_{\mathrm{XC}}^{\mathrm{MGGA}}\left(\rho(\mathbf{r}), \nabla\rho(\mathbf{r}), \tau(\mathbf{r})\right) = \int f\left[\rho(\mathbf{r}), \nabla\rho(\mathbf{r}), \tau(\mathbf{r})\right] \mathrm{d}\mathbf{r}. \tag{2.13}$$

The exchange part is slightly modified compared to its GGA counterpart by making the enhancement factor also dependent on the kinetic energy density:

$$E_{\mathrm{X}}^{\mathrm{MGGA}}\left(\rho(\mathbf{r}), \nabla\rho(\mathbf{r}), \tau(\mathbf{r})\right) = \int \rho(\mathbf{r})\epsilon_{\mathrm{X}}(\rho(\mathbf{r}))F(s, \tau(\mathbf{r}))\,\mathrm{d}\mathbf{r}, \tag{2.14}$$

where the functional form of the enhancement factor again depends on the specific DF. In the "made simple" (MS) scheme[21], the enhancement factor is defined as

$$F^{\mathrm{MS}}(s, \alpha) = F^1(s) + f(\alpha)(F^0(s; c) - F^1(s)), \tag{2.15}$$

where $F^1(s)$ and $F^0(s; c)$ are the enhancement factors for the jellium and single-orbital cases, respectively, which are only dependent on the gradient of the electron density. The interpolation function $f(\alpha)$ depends on $\tau(\mathbf{r})$ through the inhomogeneity parameter

$$\alpha = \frac{\tau(\mathbf{r}) - \tau^{\mathrm{W}}(\mathbf{r})}{\tau^{\mathrm{jellium}}(\mathbf{r})}, \tag{2.16}$$

where τ^{jellium} is the kinetic energy density for the jellium, and τ^{W} is the von Weizsäcker kinetic energy density for the single-orbital electron density. Crucially, with the α parameter a distinction can be made between a molecular orbital regime ($\alpha \approx 0$), a metalic orbital regime ($\alpha \approx 1$), and a weakly bonding regime ($\alpha \gg 1$), which allows for the design of a DF that is able to be accurate for both molecules and solids. This accurate description of the different density regimes can be achieved through switching between the F^0 and F^1 enhancement factors using a specific form for the interpolation function, e.g.[21],

$$f(\alpha) = \frac{1 - \alpha^2}{1 + \alpha^3 + b\alpha^6}, \tag{2.17}$$

where b is a constant dependent on the DF design, and, here, is taken to be equal to one. Again, the form of the enhancement factor is dependent on the design of the DF, of which the PBE-like (MS-PBEl) and RPBE-like (MS-RPBEl)

expressions are highlighted here:

$$F^1_{\mathrm{PBE}}(s) = 1 + \kappa\left(1 - \frac{1}{1 + \mu s^2/\kappa}\right), \tag{2.18}$$

$$F^1_{\mathrm{RPBE}}(s) = 1 + \kappa\left(1 - e^{-\mu s^2/\kappa}\right). \tag{2.19}$$

Note that for the MS-PBEl and MS-RPBEl DFs $\kappa = 0.804$ (i.e., the value for (R)PBE) and $\mu = 10/81$. The μ value is taken from PBEsol[22], as is appropriate for metallic electron densities[23], and not from (R)PBE. This way, in metallic bonding regimes, the MS-(R)PBEl DF performs (almost) as well as the PBEsol DF, which yields excellent results for metals. Furthermore, F^0 can be obtained by simply replacing μs^2 with $(\mu s^2 + c)$. Subsequently, this c parameter is optimized to ensure that the DF reproduces the exact exchange energy for the free hydrogen atom, yielding an approximate correction in the molecular orbital regime for the self-interaction error (SIE) fundamental to DFT[24]. Moreover, since the correlation functional for MGGA DFs is a rather large expression, the reader is referred to, e.g., Refs. [25] (TPSS) and [26] (revTPSS, which is used in the MS DFs). Nevertheless, $E_{\mathrm{C}}^{\mathrm{MGGA}}$ is extended from $E_{\mathrm{C}}^{\mathrm{GGA}}$ in a similar way as has been done for $E_{\mathrm{X}}^{\mathrm{MGGA}}$.

Non-local Exchange

Another potential route to improve DFs is to go from a semi-local to a non-local functional. This way, the error in the non-local classical self-interaction can be corrected for since a non-local XC energy is required to do so[27]. One way to achieve this is by replacing a part of the local DFT exchange with Hartree-Fock (HF) exact exchange, yielding a so-called hybrid DF. The most commonly used hybrid DFs (e.g., B3LYP[28] and PBE0[29]) are the global hybrid DFs, where a fixed ratio α_{X} of HF and DFT exchange is employed, while keeping the full DFT correlation energy:

$$E_{\mathrm{XC}}^{\mathrm{Hybrid}} = \alpha_{\mathrm{X}} E_{\mathrm{X}}^{\mathrm{HF}} + (1 - \alpha_{\mathrm{X}}) E_{\mathrm{X}}^{\mathrm{DFT}} + E_{\mathrm{C}}^{\mathrm{DFT}}. \tag{2.20}$$

Note that these hybrid DFs are often used with GGA DFs, but can in principle be combined with any type of (semi-)local DF (e.g., MGGA). However, global hybrid DFs yield an incorrect description of the long-range Coulomb interaction, which can be especially catastrophic for extended systems such as metals. Therefore, screened hybrid DFs have been developed that do yield the correct asymptotic behaviour. This screening is the result of separating the Coulomb operator in a short-range (SR) and long-range (LR) part, which usually leads

to the following operator[30–32]:

$$\frac{1}{r_{12}} = \underbrace{\frac{\mathrm{erfc}(\omega r_{12})}{r_{12}}}_{\mathrm{SR}} + \underbrace{\frac{\mathrm{erf}(\omega r_{12})}{r_{12}}}_{\mathrm{LR}}, \tag{2.21}$$

where r_{12} is the interelectronic distance and ω is the screening length parameter. ω can then be determined empirically by fitting databases[32, 33], optimally tuned to reproduce physical constraints for ionization potentials[34–37], or optimized to ensure the reproduction of the energy of a free hydrogen atom[38, 39]. The total XC energy can then be expressed as

$$E_{\mathrm{XC}}^{\text{Screened hybrid}} = \alpha_{\mathrm{X}} E_{\mathrm{x,HF}}^{\mathrm{SR}} + (1-\alpha_{\mathrm{X}}) E_{\mathrm{x,DFT}}^{\mathrm{SR}} + E_{\mathrm{x,DFT}}^{\mathrm{LR}} + E_{\mathrm{c,DFT}}. \tag{2.22}$$

In addition to retrieving the correct asymptotic behaviour for the Coulomb interaction, a screened hybrid DF also lowers the computational cost considerably for an extended system, making screened hybrid DFs tractable for metal systems. However, it should also be noted that while including HF exchange diminishes the SIE, at the same time it introduces a static correlation error as well, especially for multi-reference systems[40]. Post HF methods employing multiple Slater determinants might be able to diminish the static correlation error while simultaneously reducing the SIE, but are at present intractable for extended systems.

Non-local Correlation

The correlation energy can also be treated non-locally. A very popular way to include non-local correlation effects is include dispersion corrections in a *a posteriori* scheme such as the empirical Grimme[41, 42] or Tkatchenko-Scheffler[43] dispersion corrections. The benefit of these a posteriori dispersion corrected DFT calculations is that the increase in the computational cost compared to non-corrected DFT calculations is negligible. Self-consistent non-local correlation DFs have also been developed, such as the vdW-DF family[44–46] and (r)VV10 DFs[47, 48]. Due to the integration of a non-local double integral, the vdW and VV10 type of DFs are considerably more expensive than dispersion corrected DFs, even with efforts to improve the efficiency with which the integral is integrated[49]. The VV10 type of DFs can be combined with any type of correlation DF as long as that DF does not include any long-range correlation effects, i.e., the DF is (semi-)local:

$$E_{\mathrm{XC}}^{\mathrm{VV10}} = E_{\mathrm{X}} + E_{\mathrm{C}}^{\text{(Semi-)Local}} + E_{\mathrm{C}}^{\mathrm{VV10}}. \tag{2.23}$$

In contrast, the vdW-DF DFs consist of a fully local correlation part (i.e., LDA correlation) in addition to a non-local correlation part:

$$E_{XC}^{\text{vdW-DF}} = E_X + E_C^{\text{LDA}} + E_C^{\text{Non-local}}. \tag{2.24}$$

Another way to include non-local correlation is to derive a correlation DF in the same way as a hybrid exchange DF by mixing DFT correlation with non-local exact partial correlation (e.g., second-order Møller-Plesset):

$$E_{XC}^{\text{Double hybrid}} = \alpha_X E_X^{\text{HF}} + (1-\alpha_X) E_X^{\text{DFT}} + \alpha_C E_C^{\text{Non-local}} (1-\alpha_C) E_C^{\text{DFT}}, \tag{2.25}$$

which is also called a double hybrid DF[50]. A single hybrid DF where only hybrid correlation is employed, and no hybrid exchange, is also possible but uncommon. Unfortunately, exact partial correlation is even more expensive than non-local vdW DFs and, so far, has been intractable to apply to molecule-metal surface reactions. The correlation mixing ratio α_C can again be optimized empirically, or from physical constraints such as the one-parameter double-hybrid approximation[51].

Specific Reaction Parameter Approach

Finally, a pragmatic semi-empirical approach in the construction of an XC-DF is the so-called specific reaction parameter (SRP) approach. In the original approach devised by Truhlar and coworkers, one or a few parameters of an XC-DF is fitted to a set of experimental data for a specific gas-phase reaction[52, 53]. Subsequently, this optimized XC-DF, or SRP-DF, can be tested against different experimental data sets for the same reaction. Kroes and coworkers have extended this approach to molecule-metal surface reactions[54, 55]. A weighted average of two DFs is used, of which the mixing ratio is again fitted against a single set of experimental data for a specific molecule-metal surface reaction. Likewise, this DF is subsequently tested for different experimental sets, and if successful, a single parameter SRP-DF is obtained. Interestingly, in some cases, such an SRP-DF is observed to even reproduce experiments for other chemically related systems, even though these systems have not been included in the fitting procedure[56].

2.1.2 Plane Wave DFT

DFT calculations require some form of basis set in order to represent the wave functions. According to Bloch's theorem[57], plane waves are a convenient

way to represent the basis set for periodic systems:

$$\psi_j(\mathbf{r},\mathbf{k}) = N \sum_{\mathbf{G}} c_{j\mathbf{Gk}} e^{i(\mathbf{k}+\mathbf{G})\mathbf{r}}, \tag{2.26}$$

where j runs over the KS orbitals, $\mathbf{k}$ is a vector in the first Brillouin zone, $\mathbf{G}$ is a reciprocal lattice vector, $c_{j\mathbf{Gk}}$ is an expansion coefficient, and N is a normalization factor. An additional advantage of a plane wave basis set is the computational ease with which the forces are calculated analytically due to the Pulay forces being zero if a basis set is employed that is independent of the ionic positions[58]. In order to have a tractable finite number of plane waves, the Brillouin zone is discretized with a k-point grid and Eq. 2.26 is truncated with a kinetic energy cut-off for the plane waves:

$$\frac{1}{2}|\mathbf{k}+\mathbf{G}|^2 \leq E_{\text{cut}}. \tag{2.27}$$

For the accuracy of the calculations, both the k-point grid and E_{cut} have to be checked for convergence. Furthermore, the strong oscillations of the wave functions of the core electrons close to the nuclei require a very large E_{cut}. Therefore, pseudopotentials are employed that replace core electrons with a smooth potential[59, 60], resulting in a reduction of E_{cut}. Moreover, since only valence electrons are treated explicitly, the computational cost is reduced even further.

2.2 Dynamics Methods

For performing (quasi-)classical trajectory ((Q)CT) calculations, forces are required to integrate Newton's equations of motion and to propagate the ions (Section 2.2.1). These forces can be obtained, e.g., directly from plane wave DFT or from a fitted PES at negligible or minimal costs, respectively (see Section 2.3).

2.2.1 Integration Algorithm

In this thesis, Newton's equations of motion are integrated with the leapfrog algorithm when employing ab initio molecular dynamics (AIMD) and VASP[60–64] (Chapters 6, 7, 9 and 10), the Bulirsch-Stoer algorithm[65, 66] when employing the corrugation reducing procedure (CRP)[67] and the inhouse-built program QCTraj (Chapter 5), or the velocity Verlet algorithm[68] when employing

a high-dimensional neural network potential (HDNNP)[69] and LAMMPS[70, 71] (Chapters 3, 4 and 8).

Velocity Verlet

In the velocity Verlet algorithm[68], first the velocity $\mathbf{v}$ is advanced with half a timestep Δt:

$$\mathbf{v}(t + \Delta t/2) = \mathbf{v}(t) + \mathbf{a}(t)\Delta t/2. \tag{2.28}$$

Subsequently, the position $\mathbf{x}$ is advanced with a full time step

$$\mathbf{x}(t + \Delta t) = \mathbf{x}(t) + \mathbf{v}(t + \Delta t/2)\Delta t, \tag{2.29}$$

from which the new acceleration $\mathbf{a}(t + \Delta t)$ is computed. Finally, the velocity is advanced with another half a timestep:

$$\mathbf{v}(t + \Delta t) = \mathbf{v}(t + \Delta t/2) + \mathbf{a}(t + \Delta t)\Delta t/2. \tag{2.30}$$

Leapfrog

The leapfrog algorithm is similar to the velocity Verlet algorithm, but the velocity and position are advanced at staggered time points, i.e., the velocity and position updates "leapfrog" each other. The advantage of the leapfrog over the velocity Verlet algorithm is that the velocity is only updated once per timestep instead of twice. However, one needs to be careful with the initial conditions (see Section 2.4) since the initial velocity is at half a time step earlier than the initial position. First, the acceleration is determined at time t, with which $\mathbf{v}(t - \Delta t/2)$ can be advanced a full time step:

$$\mathbf{v}(t + \Delta t/2) = \mathbf{v}(t - \Delta t/2) + \mathbf{a}(t)\Delta t. \tag{2.31}$$

Then, the position can be propagated:

$$\mathbf{x}(t + \Delta t) = \mathbf{x}(t) + \mathbf{v}(t + \Delta t/2)\Delta t. \tag{2.32}$$

Bulirsch-Stoer

The Bulirsch-Stoer algorithm[65, 66] is more involved and is therefore only briefly discussed. Initially, a large timestep H is chosen. Then, H is subdivided in n pieces, or smaller timesteps, after which the position at $t + H$ is determined through polynomial extrapolation towards an infinite number of timesteps within H, i.e., $\Delta t \to 0$ and $n \to \infty$. This subdivision is repeated with

an increasing number of timesteps using the sequence[72, 73]

$$n_j = 2, 4, 6, \ldots, 2j, \ldots, 2j_{\max}, \tag{2.33}$$

where j indicates the iteration. If the estimated error associated with the extrapolation is sufficiently low, the integration is considered to be accurate and the position is updated. If the desired accuracy is not achieved within $j_{\max}$ iterations, H is halved and the procedure is repeated. The advantage of the Bulirsch-Stoer integrator is that it allows for adaptive timesteps and concomitant reduction in computational time while maintaining the desired accuracy.

2.2.2 (Quasi-)Classical and Quantum Dynamics

Nowadays, QCT is preferred over CT for molecule-metal surface reactions since QCT generally yields results in good agreement with quantum dynamics (QD)[74–77]. The good performance of QCT is achieved by including the quantum mechanical vibrational zero-point energy (ZPE) in the initial conditions (see also Section 2.4.2), opposed to CT where ZPE is not included. Note that occasionally CT outperforms QCT, but this is caused by artificial ZPE leakage in the QCT approach[78, 79]. However, when quantum effects such as tunneling play an important role, the QCT approach often fails, especially for (light) molecules with a total kinetic energy below the barrier height. Full dimensional QD simulations would include all quantum effects, but are intractable due to the large number of degrees of freedom (DOFs) and concomitant computational cost. Therefore, surface atom motion is not included in QD and QD simulations are limited to small molecules or reduced dimensionality Hamiltonians. One way to include quantum effects in simulations with a large number of DOFs is to employ ring polymer molecular dynamics (RPMD)[75, 80, 81]. However, RPMD is computationally still demanding due to its linear scaling with the number of beads, especially at low temperatures (the number of beads required to approximate QD scales inversely with the temperature), and remains largely untested for molecule-metal surface reactions[75]. Fortunately, precomputed PESs and the generally high temperatures involved in molecule-metal surface reactions allow for tractable RPMD calculations.

2.3 Fitting Potential Energy Surfaces

Evaluation of the forces required for MD can be performed *ab initio* (i.e., on-the-fly) with DFT, which is commonly referred to as ab initio molecu-

lar dynamics (AIMD), density functional molecular dynamics (DFMD), or Born-Oppenheimer molecular dynamics (BOMD). The large advantages of performing AIMD are that no prior knowledge of the dynamics is required and that many degrees of freedom can be modeled explicitly, which tends to be complicated or unfeasible in procedures that fit or interpolate the PES. However, due to the associated computational costs, AIMD calculations are limited in both the system size and amount of trajectories. This is especially problematic for molecule-metal surface reactions with low reactivity (i.e., $< 1\%$) in that it limits the statistical accuracy with which these probabilities can be calculated. Therefore, many different approaches have been developed where the PES is precomputed and subsequently fitted, leading to a considerable reduction in computational cost. Two different approaches are discussed here, namely the CRP[67] and Behler-Parrinello approach to neural network potentials[69]. Both approaches are capable of fitting or interpolating a PES with chemical accuracy, i.e., with an RMSE lower than 4.2 kJ/mol.

2.3.1 Corrugation Reducing Procedure (CRP)

A 6D PES for a diatomic molecule interacting with a metal surface can be easily constructed with the CRP[67]. The accuracy of this method comes from a procedure that reduces the energetic corrugation of the 6D function that is interpolated. This reduction is achieved by subtracting the single atom-surface PESs (i.e., the 3D PES V_i^{3D}) from the molecular PES (i.e., the full 6D PES V^{6D}), yielding the smoother 6D interpolation function I^{6D}:

$$I^{6D}(\mathbf{R}, \mathbf{q}) = V^{6D}(\mathbf{R}, \mathbf{q}) - \sum_{i=1}^{2} V_i^{3D}(\mathbf{r}_i), \tag{2.34}$$

where $\mathbf{R}$ is the vector of the cartesian coordinates of the center of mass (i.e., X, Y and Z) and $\mathbf{q}$ is the vector of the spherical internal coordinates of the molecule (i.e., r, θ and ϕ) Subsequently, I^{6D} can be interpolated. Similarly, the atom-surface PES can also be made smoother prior to the interpolation by subtracting a sum of potentials for each atom in the molecule interacting with the surface atoms:

$$I_A^{3D}(\mathbf{R}) = V_A^{3D}(\mathbf{R}) - \sum_{j=1}^{N} V^{1D}\left(R_{A,j}\right). \tag{2.35}$$

Here, $V^{1D}\left(R_{A,j}\right)$ is taken to be directly above the top site, $R_{A,j}$ is the distance between the surface atom j and atom A, and N is the number of surface atoms

in the reference cluster. For the evaluation of the energy from the full 6D PES, the atom-surface PESs are added back to the interpolated PES:

$$V^{6D}(\mathbf{R},\mathbf{q}) = I^{6D}(\mathbf{R},\mathbf{q}) + \sum_{i=1}^{2} V_i^{3D}(\mathbf{r}_i)\,. \tag{2.36}$$

Likewise, the same procedure is employed for the atom-surface interaction energy. In the construction of the DFT data set employed in the interpolation, the symmetry of both the surface and the molecule are taken into account in order to reduce the size of the data set and concomitant computational effort. Another benefit of this approach is that it is general, i.e., it can be employed for any diatomic molecule and surface. In principle the CRP can also be extended to polyatomic molecules, however, the increase in degrees of freedom would severely complicate the applied symmetry, increase the data set size, and no guarantee exists that the PES would be sufficiently smooth for the interpolation.

2.3.2 Behler-Parrinello Approach to High-Dimensional Neural Network Potentials (HD-NNPs)

A procedure for obtaining a fit of the potential for a high-dimensional system that is relatively cheap from a computational point of view is the HD-NNP approach proposed by Behler and Parrinello[69]. The benefit of this approach is that it is system-size independent and allows for tractable simulations while explicitly modeling surface atom motion. In the HD-NNP, the total energy is evaluated as a sum of atomic contributions that are dependent on their energetically relevant local environment, which is described by many-body atom-centered symmetry functions[82]. Considering that the used symmetry functions and fitting procedure have been described in earlier studies[69, 82–85], only a short summary is given here for the symmetry functions[82]. The local environment of an atom is defined by the following cut-off function

$$f_c(R) = \begin{cases} \frac{1}{2}\left[\cos\left(\pi\frac{R}{R_c}\right)+1\right] & R < R_c \\ 0 & R \geq R_c, \end{cases} \tag{2.37}$$

where only atomic contributions within the cut-off radius are taken into account. This cut-off radius needs to be large enough to ensure that long-range interactions are included as well, but not too large in order to avoid interactions with periodic images. The radial symmetry functions (effectively

two-body interactions) are[69, 82]

$$G_i^2 = \sum_{j \neq i} e^{-\eta(R_{i,j}-R_s)^2} f_c(R_{i,j}), \tag{2.38}$$

where $R_{i,j}$ is the internuclear distance between atoms i and j, and η and R_s are parameters characterizing the function form, for which $R_s = 0$ in this thesis. Furthermore, the angular symmetry functions (effectively three-body interactions) are taken as[69, 82]

$$G_i^4 = 2^{1-\zeta} \sum_{j,k \neq i} (1 + \lambda \cos\theta_{i,j,k})^{\zeta} e^{-\eta(R_{i,j}+R_{i,k}+R_{j,k})} f_c(R_{i,j}) f_c(R_{i,k}) f_c(R_{j,k}), \tag{2.39}$$

where $\theta_{i,j,k} = \frac{R_{i,j} \cdot R_{i,k}}{R_{i,j} R_{i,k}}$, and η, ζ and λ are parameters characterizing the function form. Note that since a summation over all two- and three-body interactions inside the cut-off radius is performed, a many-body description is achieved.

2.4 Initial Condition Sampling

Accurate simulations of experiments require one to faithfully represent the experiment, and thus special consideration of the initial conditions in MD simulations is required. Here, the initial conditions of both the metal surface and molecular beam are discussed in order to accurately simulate reactive scattering of molecules on metal surfaces.

2.4.1 Metal Surface

In order to simulate the effect of surface temperature (T_s), a procedure can be employed as described in Refs. [55] and [86]. An independent 1D harmonic oscillator model is used to mimic the local distortion of the ideal surface and the thermal motion of the surface atoms, by assigning initial displacements and velocities to the atoms of the mobile layers. Using $K = 1/2mv^2$ and $U = 1/2kx^2$, where K and U are the kinetic and potential energies, respectively, the following Boltzmann distributions for the velocities and positions are obtained:

$$f(v) = \left(\frac{m}{2\pi k_B T}\right)^{\frac{1}{2}} e^{\frac{-mv^2}{2k_B T}} \tag{2.40}$$

$$f(q) = \left(\frac{m\omega^2}{2\pi k_B T}\right)^{\frac{1}{2}} e^{\frac{-m\omega^2 q^2}{2k_B T}} \tag{2.41}$$

The frequency ω is obtained by performing normal mode calculations for a single atom in an ideal metal slab, which are performed for each of the mobile layers. This yields the frequencies that are employed in the aforementioned Boltzmann distributions. Furthermore, the theoretically computed lattice constant is expanded by an experimentally obtained lattice expansion coefficient in order to account for the thermal expansion from $T_s = 0\,\mathrm{K}$ to the simulated surface temperature[87]. Several differently-initialized slabs are generated using the aforementioned procedure, which are then equilibrated for 2 ps by doing NVE (constant number of particles, volume and total energy) MD runs with an 1 fs time step and allowing the atoms in the mobile layers to move in all directions. The configurations (positions and velocities) in the last picosecond of these simulations are then used to form a pool of initial conditions. Typically, the atoms in the bottom layer(s) of the metal slab are kept fixed in their ideal positions during the calculations.

2.4.2 Molecular Beam

Molecular beam experiments are typically simulated by reproducing both the rovibrational state and the velocity distributions present in the experiment. The rovibrational state population $F_{v_i,j}$ of a molecule in the molecular beam is given by

$$F_{v,j}\left(T_\mathrm{n}\right) = \frac{2j+1}{Z\left(T_\mathrm{n}\right)} \exp\left(-\frac{\left(E_{v_i,0} - E_{0,0}\right)}{k_\mathrm{B} T_\mathrm{vib}}\right) \exp\left(-\frac{\left(E_{v_i,j} - E_{v_i,0}\right)}{k_\mathrm{B} T_\mathrm{rot}}\right), \tag{2.42}$$

where $Z\left(T_\mathrm{n}\right)$ is the partition function and T_n, T_vib, and T_rot are the nozzle, vibrational, and rotational temperatures, respectively.

Throughout this thesis, molecules are treated as either a linear rigid rotor (in this thesis HCl and O_2) or an oblate symmetric top rigid rotor (in this thesis NH_3, CHD_3, and, after application of an appropriate approximation, CH_3OH) for the sampling of the rotational state[88]. Here, the two quantum numbers J and M define the orientation of the angular momentum vector in a space fixed reference frame, where the Z axis (i.e., the vector normal to the surface plane) is fixed in space. J corresponds to the total rotational angular momentum $\mathbf{L}$ and M to its projection on the Z axis:

$$|\mathbf{L}| = \hbar\sqrt{J\left(J+1\right)}, \tag{2.43}$$

$$\mathbf{L}_Z = \hbar M. \tag{2.44}$$

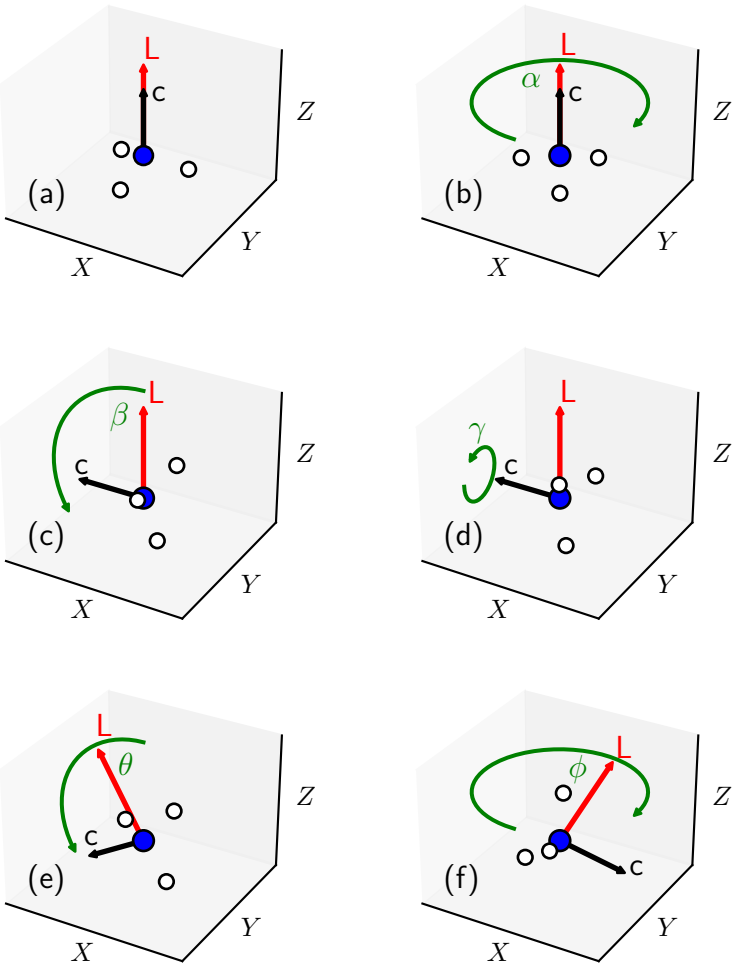

FIGURE 2.1: (a) The initial orientation of an oblate symmetric top molecule (black arrow), here an ammonia molecule, and its angular momentum vector (red arrow) are fixed with respect to the space fixed reference frame (XYZ). (b-f) Same as panel a, but indicating the rotations (green arrows) of the molecular orientation and the angular momentum vectors required according to the quantum numbers J, M, and K. See the text for the meaning of the rotations.

Additionally, the quantum number K fixes the orientation of the figure axis (here, taken to be the principle axis **C**) with respect to the angular momentum vector:

$$\mathbf{L}_{\text{figure}} = \hbar K, \tag{2.45}$$

Furthermore, M and K are integers in the range $[-J, +J]$. Note that K is only relevant for the symmetric top rotor as the linear rotor obviously does not rotate about its intramolecular (figure) axis. The orientation of the molecule and the angular momentum vector can then be obtained as follows. First, both the figure axis **C** of the molecule and the angular momentum vector **L** are oriented parallel to the surface normal Z (Figure 2.1a). Then, the figure axis is rotated by the α, β, and γ Euler angles using the ZYZ convention (Figures 2.1b-d, respectively). The rotations by the α and γ angles are both in the interval $[0, 2\pi]$. The angle β is computed from J and K as follows:

$$\cos(\beta) = \frac{K}{\sqrt{J(J+1)}}. \tag{2.46}$$

Finally, both the figure axis and the angular momentum vector are rotated by the spherical θ and ϕ angles (Figures 2.1e,f, respectively) about the Z axis. The polar angle θ is computed from J and M as follows:

$$\cos(\theta) = \frac{M}{\sqrt{J(J+1)}}. \tag{2.47}$$

The azimuthal angle is in the interval $\phi \in [0, 2\pi]$ (or $\phi \in [0, 2\pi/2n]$ when taking into account the C_{nv} symmetry of the molecule). If $J = 0$, one can simply obtain the molecular orientation by randomly sampling β from a $\sin(\beta)$ distribution, and α and γ from the $[0, 2\pi]$ interval, where the angular momentum is zero (i.e., $|\mathbf{L}| = 0$).

The vibrational state of a molecule is obtained by performing a micro-canonical sampling for each of its vibrational modes. An 1D QCT simulation is performed along each mode, from which the initial displacement (compared to the equilibrium geometry) and concomitant velocity is selected by randomly sampling the phase of the vibration. Subsequently, the sum of displacements and velocities are added to the atomic positions and velocities, while also taking into account the orientation of the molecule given by its rotational state.

The center of mass (COM) velocity v of the molecule in the molecular beam is given by the flux weighted probability distribution[89, 90]

$$f(v; T_{\text{n}})\, \mathrm{d}v = A v^3 e^{-(v-v_0)^2/\alpha^2}\, \mathrm{d}v, \tag{2.48}$$

where A is a normalization constant, v_0 is the stream velocity, and α is the width of the distribution.

In order to keep DFT calculations tractable, often a smaller vacuum distance is employed than what would be considered to be converged. This is typically the case when a Van der Waals correlation DF is employed since the Van der Waals interactions cause long-range interaction between the molecule and metal surface. The interaction energy, defined as $E_R = E_b^{\text{small vacuum}} - E_b^{\text{large vacuum}}$, at a large distance between the molecule and the metal surface is only dependent on the molecular coordinate Z, i.e., the distance between the molecule and the metal surface. To correct for the artificial increase in barrier height due to the interaction energy, this energy is added to the initial velocity ($v = \sqrt{2E/M_{\text{molecule}}}$) of the molecule, similar to what has been done and justified in previous work[55].

Finally, the molecule's center of mass is placed halfway between the two periodic slabs (i.e., the value of Z is half of the vacuum distance) and samples randomly the entire unit cell in X and Y.

2.5 Calculation of Observables

Here, the computation of several observables in MD simulations is discussed. First, three different possible outcomes have been defined for MD simulations, i.e., scattering, reaction and trapping. A molecule is considered to be scattered when the value of Z for the center of mass is larger than half of the vacuum distance (i.e., larger than as in the initial conditions) and its momentum is pointing away from the surface. Furthermore, throughout this thesis, the molecule is considered to be reacted if one of the intramolecular bonds is either longer than 3 Å, or longer than 2 Å for 100 fs, unless noted otherwise. Finally, if none of the aforementioned results are obtained within the simulation time, the molecule is considered to be trapped.

The reaction probability p is defined as $p = N_r/N_i$, where N_r and N_i are the amount of reacted and initial trajectories, respectively. Similarly, the sticking probability S_0, which includes contributions of both reacted and trapped trajectories, is defined as $S_0 = (N_r + N_t)/N_i$, where N_t is the amount of trapped trajectories. The standard deviation of probabilities is $\sigma = \sqrt{p(1-p)/N}$, where N is the sample size. However, for probabilities that are 0 or 100% the one-sided interval $\alpha^{1/N}$ is used[91], where α is the confidence interval.

Vibrational (χ_v) and rotational (χ_J) efficacies indicate how effective it is to promote the reaction by increasing the vibrational and rotational energy compared to increasing the translational energy. This efficacy is computed as

follows:

$$\chi_\nu(J, \langle E_\mathrm{i} \rangle) = \frac{\langle E_\mathrm{i}(\nu = 0, J; S_0) \rangle - \langle E_\mathrm{i}(\nu, J; S_0) \rangle}{E_\mathrm{vib}(\nu, J) - E_\mathrm{vib}(\nu = 0, J)}, \tag{2.49}$$

$$\chi_J(\nu, \langle E_\mathrm{i} \rangle) = \frac{\langle E_\mathrm{i}(\nu, J = 0; S_0) \rangle - \langle E_\mathrm{i}(\nu, J; S_0) \rangle}{E_\mathrm{rot}(\nu, J) - E_\mathrm{rot}(\nu, J = 0)}, \tag{2.50}$$

where it is assumed that S_0 is a bijective or invertible function, i.e., only one value of E_i corresponds to a particular value of S_0. This will usually be true as S_0 tends to be a monotonically increasing function of E_i.

The energy transfer E_T from the molecule to the metal surface is defined as

$$E_\mathrm{T} = (V_\mathrm{i} + K_\mathrm{i}) - (V_\mathrm{f} + K_\mathrm{f}), \tag{2.51}$$

where V and K are the potential electronic and kinetic energy of the molecule, respectively, at the initial (i) and final (f) time steps of the scattered trajectories. The hard sphere Baule model[92] is often used to provide a rough prediction of the energy transfer, where the mass ratio between the molecule and the surface atom plays a large role in the energy transfer. This energy transfer is described by

$$E_\mathrm{T} = \frac{4\mu \cos^2 \gamma}{(1+\mu)^2} \langle E_\mathrm{i} \rangle , \tag{2.52}$$

where $\mu = m/M$ (m is the mass of the projectile and M is the mass of a surface atom), γ is the angle between the velocity vector of the molecule and the line connecting the centers of the hard spheres of the molecule and surface atom at impact, and $\langle E_\mathrm{i} \rangle$ is the average incidence energy. In general, it is observed that the lower the surface atom mass is, the higher the energy transfer is from the molecule to the surface atoms due to the masses of the molecule and the surface atom being more similar. Typically, the Baule model is actually taken as an upper limit by treating the collision as a head-on collision ($\gamma = 0$), from which one obtains the well-known Baule limit

$$E_\mathrm{T} = \frac{4\mu}{(1+\mu)^2} \langle E_\mathrm{i} \rangle . \tag{2.53}$$

However, when an empirical average for the γ angle distribution is used, in what here is called the refined Baule model, the following equation for the average energy transfer is obtained[93]:

$$\langle E_\mathrm{T} \rangle = \frac{2.4\mu}{(1+\mu)^2} \langle E_\mathrm{i} \rangle . \tag{2.54}$$

References

(1) Born, M.; Oppenheimer, R. Zur Quantentheorie Der Molekeln. *Ann. Phys.* **1927**, *389*, 457–484, DOI: 10.1002/andp.19273892002.

(2) Hohenberg, P.; Kohn, W. Inhomogeneous Electron Gas. *Phys. Rev.* **1964**, *136*, B864–B871, DOI: 10.1103/PhysRev.136.B864.

(3) Kohn, W.; Sham, L. J. Self-Consistent Equations Including Exchange and Correlation Effects. *Phys. Rev.* **1965**, *140*, A1133–A1138, DOI: 10.1103/PhysRev.140.A1133.

(4) Perdew, J. P.; Schmidt, K. Jacob's Ladder of Density Functional Approximations for the Exchange-Correlation Energy. *AIP Conf. Proc.* **2001**, *577*, 1–20, DOI: 10.1063/1.1390175.

(5) Dirac, P. a. M. Note on Exchange Phenomena in the Thomas Atom. *Math. Proc. Camb. Philos. Soc.* **1930**, *26*, 376–385, DOI: 10.1017/S0305004100016108.

(6) Alder, B.; Ceperly, D. Ground State of the Electron Gas by a Stochastic Method. *Phys. Rev. Lett.* **1980**, *45*, 566–569, DOI: 10.1103/PhysRevLett.45.566.

(7) Vosko, S. H.; Wilk, L.; Nusair, M. Accurate Spin-Dependent Electron Liquid Correlation Energies for Local Spin Density Calculations: A Critical Analysis. *Can. J. Phys.* **1980**, *58*, 1200–1211, DOI: 10.1139/p80-159.

(8) Perdew, J. P.; Zunger, A. Self-Interaction Correction to Density-Functional Approximations for Many-Electron Systems. *Phys. Rev. B* **1981**, *23*, 5048–5079, DOI: 10.1103/PhysRevB.23.5048.

(9) Perdew, J. P.; Wang, Y. Accurate and Simple Analytic Representation of the Electron-Gas Correlation Energy. *Phys. Rev. B* **1992**, *45*, 13244–13249, DOI: 10.1103/PhysRevB.45.13244.

(10) Chachiyo, T. Communication: Simple and Accurate Uniform Electron Gas Correlation Energy for the Full Range of Densities. *J. Chem. Phys.* **2016**, *145*, 021101, DOI: 10.1063/1.4958669.

(11) Peverati, R.; Truhlar, D. G. Exchange–Correlation Functional with Good Accuracy for Both Structural and Energetic Properties While Depending Only on the Density and Its Gradient. *J. Chem. Theory Comput.* **2012**, *8*, 2310–2319, DOI: 10.1021/ct3002656.

(12) Peverati, R.; Truhlar, D. G. Quest for a Universal Density Functional: The Accuracy of Density Functionals across a Broad Spectrum of Databases in Chemistry and Physics. *Philos. Trans. R. Soc. A* **2014**, *372*, 20120476, DOI: 10.1098/rsta.2012.0476.

(13) Perdew, J. P.; Burke, K.; Ernzerhof, M. Generalized Gradient Approximation Made Simple. *Phys. Rev. Lett.* **1996**, *77*, 3865–3868, DOI: 10.1103/PhysRevLett.77.3865.

(14) Hammer, B.; Hansen, L. B.; Nørskov, J. K. Improved Adsorption Energetics within Density-Functional Theory Using Revised Perdew-Burke-Ernzerhof Functionals. *Phys. Rev. B* **1999**, *59*, 7413–7421, DOI: 10.1103/PhysRevB.59.7413.

(15) Lieb, E. H.; Oxford, S. Improved Lower Bound on the Indirect Coulomb Energy. *Int. J. Quantum Chem.* **1981**, *19*, 427–439, DOI: 10.1002/qua.560190306.

(16) Odashima, M. M.; Capelle, K.; Trickey, S. B. Tightened Lieb-Oxford Bound for Systems of Fixed Particle Number. *J. Chem. Theory Comput.* **2009**, *5*, 798–807, DOI: 10.1021/ct8005634.

(17) Seidl, M.; Vuckovic, S.; Gori-Giorgi, P. Challenging the Lieb–Oxford Bound in a Systematic Way. *Mol. Phys.* **2016**, *114*, 1076–1085, DOI: 10.1080/00268976.2015.1136440.

(18) Perdew, J. P.; Ruzsinszky, A.; Csonka, G. I.; Vydrov, O. A.; Scuseria, G. E.; Constantin, L. A.; Zhou, X.; Burke, K. Perdew et al. Reply: *Phys. Rev. Lett.* **2008**, *101*, 239702, DOI: 10.1103/PhysRevLett.101.239702.

(19) Śmiga, S.; Constantin, L. A.; Della Sala, F.; Fabiano, E. The Role of the Reduced Laplacian Renormalization in the Kinetic Energy Functional Development. *Computation* **2019**, *7*, 65, DOI: 10.3390/computation7040065.

(20) Perdew, J. P.; Constantin, L. A. Laplacian-Level Density Functionals for the Kinetic Energy Density and Exchange-Correlation Energy. *Phys. Rev. B* **2007**, *75*, 155109, DOI: 10.1103/PhysRevB.75.155109.

(21) Sun, J.; Xiao, B.; Ruzsinszky, A. Communication: Effect of the Orbital-Overlap Dependence in the Meta Generalized Gradient Approximation. *J. Chem. Phys.* **2012**, *137*, 051101, DOI: 10.1063/1.4742312.

(22) Perdew, J. P.; Ruzsinszky, A.; Csonka, G. I.; Vydrov, O. A.; Scuseria, G. E.; Constantin, L. A.; Zhou, X.; Burke, K. Restoring the Density-Gradient Expansion for Exchange in Solids and Surfaces. *Phys. Rev. Lett.* **2008**, *100*, 136406, DOI: 10.1103/PhysRevLett.100.136406.

(23) Antoniewicz, P. R.; Kleinman, L. Kohn-Sham Exchange Potential Exact to First Order in $\rho(K \to)/\rho_0$. *Phys. Rev. B* **1985**, *31*, 6779–6781, DOI: 10.1103/PhysRevB.31.6779.

(24) Perdew, J. P.; Ruzsinszky, A.; Constantin, L. A.; Sun, J.; Csonka, G. I. Some Fundamental Issues in Ground-State Density Functional Theory: A Guide for the Perplexed. *J. Chem. Theory Comput.* **2009**, *5*, 902–908, DOI: 10.1021/ct800531s.

(25) Tao, J.; Perdew, J. P.; Staroverov, V. N.; Scuseria, G. E. Climbing the Density Functional Ladder: Nonempirical Meta–Generalized Gradient Approximation Designed for Molecules and Solids. *Phys. Rev. Lett.* **2003**, *91*, 146401, DOI: 10.1103/PhysRevLett.91.146401.

(26) Perdew, J. P.; Ruzsinszky, A.; Csonka, G. I.; Constantin, L. A.; Sun, J. Workhorse Semilocal Density Functional for Condensed Matter Physics and Quantum Chemistry. *Phys. Rev. Lett.* **2009**, *103*, 026403, DOI: 10.1103/PhysRevLett.103.026403.

(27) Perdew, J. P.; Ruzsinszky, A.; Tao, J.; Staroverov, V. N.; Scuseria, G. E.; Csonka, G. I. Prescription for the Design and Selection of Density Functional Approximations: More Constraint Satisfaction with Fewer Fits. *J. Chem. Phys.* **2005**, *123*, 062201, DOI: 10.1063/1.1904565.

(28) Stephens, P. J.; Devlin, F. J.; Chabalowski, C. F.; Frisch, M. J. Ab Initio Calculation of Vibrational Absorption and Circular Dichroism Spectra Using Density Functional Force Fields. *J. Phys. Chem.* **1994**, *98*, 11623–11627, DOI: 10.1021/j100096a001.

(29) Adamo, C.; Barone, V. Toward Reliable Density Functional Methods without Adjustable Parameters: The PBE0 Model. *J. Chem. Phys.* **1999**, *110*, 6158–6170, DOI: 10.1063/1.478522.

(30) Leininger, T.; Stoll, H.; Werner, H.-J.; Savin, A. Combining Long-Range Configuration Interaction with Short-Range Density Functionals. *Chem. Phys. Lett.* **1997**, *275*, 151–160, DOI: 10.1016/S0009-2614(97)00758-6.

(31) Iikura, H.; Tsuneda, T.; Yanai, T.; Hirao, K. A Long-Range Correction Scheme for Generalized-Gradient-Approximation Exchange Functionals. *J. Chem. Phys.* **2001**, *115*, 3540–3544, DOI: 10.1063/1.1383587.

(32) Heyd, J.; Scuseria, G. E.; Ernzerhof, M. Hybrid Functionals Based on a Screened Coulomb Potential. *J. Chem. Phys.* **2003**, *118*, 8207–8215, DOI: 10.1063/1.1564060.

(33) Krukau, A. V.; Vydrov, O. A.; Izmaylov, A. F.; Scuseria, G. E. Influence of the Exchange Screening Parameter on the Performance of Screened Hybrid Functionals. *J. Chem. Phys.* **2006**, *125*, 224106, DOI: 10.1063/1.2404663.

(34) Baer, R.; Livshits, E.; Salzner, U. Tuned Range-Separated Hybrids in Density Functional Theory. *Annu. Rev. Phys. Chem.* **2010**, *61*, 85–109, DOI: 10.1146/annurev.physchem.012809.103321.

(35) Refaely-Abramson, S.; Sharifzadeh, S.; Govind, N.; Autschbach, J.; Neaton, J. B.; Baer, R.; Kronik, L. Quasiparticle Spectra from a Nonempirical Optimally Tuned Range-Separated Hybrid Density Functional. *Phys. Rev. Lett.* **2012**, *109*, 226405, DOI: 10.1103/PhysRevLett.109.226405.

(36) Karolewski, A.; Kronik, L.; Kümmel, S. Using Optimally Tuned Range Separated Hybrid Functionals in Ground-State Calculations: Consequences and Caveats. *J. Chem. Phys.* **2013**, *138*, 204115, DOI: 10.1063/1.4807325.

(37) Tamblyn, I.; Refaely-Abramson, S.; Neaton, J. B.; Kronik, L. Simultaneous Determination of Structures, Vibrations, and Frontier Orbital Energies from a Self-Consistent Range-Separated Hybrid Functional. *J. Phys. Chem. Lett.* **2014**, *5*, 2734–2741, DOI: 10.1021/jz5010939.

(38) Brémond, É.; Pérez-Jiménez, Á. J.; Sancho-García, J. C.; Adamo, C. Range-Separated Hybrid Density Functionals Made Simple. *J. Chem. Phys.* **2019**, *150*, 201102, DOI: 10.1063/1.5097164.

(39) Brémond, É.; Pérez-Jiménez, Á. J.; Sancho-García, J. C.; Adamo, C. Range-Separated Hybrid and Double-Hybrid Density Functionals: A Quest for the Determination of the Range-Separation Parameter. *J. Chem. Phys.* **2020**, *152*, 244124, DOI: 10.1063/5.0010976.

(40) Handy, N. C.; Cohen, A. J. A Dynamical Correlation Functional. *J. Chem. Phys.* **2002**, *116*, 5411–5418, DOI: 10.1063/1.1457432.

(41) Grimme, S. Accurate description of van der Waals complexes by density functional theory including empirical corrections. *J. Comput. Chem.* **2004**, *25*, 1463–1473, DOI: 10.1002/jcc.20078.

(42) Grimme, S.; Antony, J.; Ehrlich, S.; Krieg, H. A Consistent and Accurate Ab Initio Parametrization of Density Functional Dispersion Correction (DFT-D) for the 94 Elements H-Pu. *J. Chem. Phys.* **2010**, *132*, 154104, DOI: 10.1063/1.3382344.

(43) Tkatchenko, A.; Scheffler, M. Accurate Molecular Van Der Waals Interactions from Ground-State Electron Density and Free-Atom Reference Data. *Phys. Rev. Lett.* **2009**, *102*, 073005, DOI: 10.1103/PhysRevLett.102.073005.

(44) Dion, M.; Rydberg, H.; Schröder, E.; Langreth, D. C.; Lundqvist, B. I. Van Der Waals Density Functional for General Geometries. *Phys. Rev. Lett.* **2004**, *92*, 246401, DOI: 10.1103/PhysRevLett.92.246401.

(45) Lee, K.; Murray, É. D.; Kong, L.; Lundqvist, B. I.; Langreth, D. C. Higher-Accuracy van Der Waals Density Functional. *Phys. Rev. B* **2010**, *82*, 081101(R), DOI: 10.1103/PhysRevB.82.081101.

(46) Chakraborty, D.; Berland, K.; Thonhauser, T. Next-Generation Non-Local van Der Waals Density Functional. *J. Chem. Theory Comput.* **2020**, *16*, 5893–5911, DOI: 10.1021/acs.jctc.0c00471.

(47) Vydrov, O. A.; Van Voorhis, T. Nonlocal van Der Waals Density Functional: The Simpler the Better. *J. Chem. Phys.* **2010**, *133*, 244103, DOI: 10.1063/1.3521275.

(48) Sabatini, R.; Gorni, T.; de Gironcoli, S. Nonlocal van Der Waals Density Functional Made Simple and Efficient. *Phys. Rev. B* **2013**, *87*, 041108(R), DOI: 10.1103/PhysRevB.87.041108.

(49) Román-Pérez, G.; Soler, J. M. Efficient Implementation of a van Der Waals Density Functional: Application to Double-Wall Carbon Nanotubes. *Phys. Rev. Lett.* **2009**, *103*, 096102, DOI: 10.1103/PhysRevLett.103.096102.

(50) Ernzerhof, M. Construction of the Adiabatic Connection. *Chem. Phys. Lett.* **1996**, *263*, 499–506, DOI: 10.1016/S0009-2614(96)01225-0.

(51) Toulouse, J.; Sharkas, K.; Brémond, E.; Adamo, C. Communication: Rationale for a New Class of Double-Hybrid Approximations in Density-Functional Theory. *J. Chem. Phys.* **2011**, *135*, 101102, DOI: 10.1063/1.3640019.

(52) Chakraborty, A.; Zhao, Y.; Lin, H.; Truhlar, D. G. Combined Valence Bond-Molecular Mechanics Potential-Energy Surface and Direct Dynamics Study of Rate Constants and Kinetic Isotope Effects for the H + C_2H_6 Reaction. *J. Chem. Phys.* **2006**, *124*, 044315, DOI: 10.1063/1.2132276.

(53) Chuang, Y.-Y.; Radhakrishnan, M. L.; Fast, P. L.; Cramer, C. J.; Truhlar, D. G. Direct Dynamics for Free Radical Kinetics in Solution: Solvent Effect on the Rate Constant for the Reaction of Methanol with Atomic Hydrogen. *J. Phys. Chem. A* **1999**, *103*, 4893–4909, DOI: 10.1021/jp990969d.

(54) Díaz, C.; Pijper, E.; Olsen, R. A.; Busnengo, H. F.; Auerbach, D. J.; Kroes, G. J. Chemically Accurate Simulation of a Prototypical Surface Reaction: H_2 Dissociation on Cu(111). *Science* **2009**, *326*, 832–834, DOI: 10.1126/science.1178722.

(55) Nattino, F.; Migliorini, D.; Kroes, G.-J.; Dombrowski, E.; High, E. A.; Killelea, D. R.; Utz, A. L. Chemically Accurate Simulation of a Polyatomic Molecule-Metal Surface Reaction. *J. Phys. Chem. Lett.* **2016**, *7*, 2402–2406, DOI: 10.1021/acs.jpclett.6b01022.

(56) Migliorini, D.; Chadwick, H.; Nattino, F.; Gutiérrez-González, A.; Dombrowski, E.; High, E. A.; Guo, H.; Utz, A. L.; Jackson, B.; Beck, R. D.; Kroes, G.-J. Surface Reaction Barriometry: Methane Dissociation on Flat and Stepped Transition-Metal Surfaces. *J. Phys. Chem. Lett.* **2017**, *8*, 4177–4182, DOI: 10.1021/acs.jpclett.7b01905.

(57) Bloch, F. Über die Quantenmechanik der Elektronen in Kristallgittern. *Z. Physik* **1929**, *52*, 555–600, DOI: 10.1007/BF01339455.

(58) In *Heterogeneous Materials: Nonlinear and Breakdown Properties and Atomistic Modeling*, Sahimi, M., Ed.; Interdisciplinary Applied Mathematics; Springer: New York, NY, 2003, pp 455–548, DOI: 10.1007/0-387-21704-5_10.

(59) Blöchl, P. E. Projector Augmented-Wave Method. *Phys. Rev. B* **1994**, *50*, 17953–17979, DOI: 10.1103/PhysRevB.50.17953.

(60) Kresse, G.; Joubert, D. From Ultrasoft Pseudopotentials to the Projector Augmented-Wave Method. *Phys. Rev. B* **1999**, *59*, 1758–1775, DOI: 10.1103/PhysRevB.59.1758.

(61) Kresse, G.; Hafner, J. Ab Initio Molecular-Dynamics Simulation of the Liquid-Metal–Amorphous-Semiconductor Transition in Germanium. *Phys. Rev. B* **1994**, *49*, 14251–14269, DOI: 10.1103/PhysRevB.49.14251.

(62) Kresse, G.; Hafner, J. Ab Initio Molecular Dynamics for Liquid Metals. *Phys. Rev. B* **1993**, *47*, 558–561, DOI: 10.1103/PhysRevB.47.558.

(63) Kresse, G.; Furthmüller, J. Efficient Iterative Schemes for Ab Initio Total-Energy Calculations Using a Plane-Wave Basis Set. *Phys. Rev. B* **1996**, *54*, 11169–11186, DOI: 10.1103/PhysRevB.54.11169.

(64) Kresse, G.; Furthmüller, J. Efficiency of Ab-Initio Total Energy Calculations for Metals and Semiconductors Using a Plane-Wave Basis Set. *Comput. Mater. Sci.* **1996**, *6*, 15–50, DOI: 10.1016/0927-0256(96)00008-0.

(65) Bulirsch, R.; Stoer, J. Numerical Treatment of Ordinary Differential Equations by Extrapolation Methods. *Numer. Math.* **1966**, *8*, 1–13, DOI: 10.1007/BF02165234.

(66) Stoer, J.; Bulirsch, R. In *Introduction to Numerical Analysis*, Stoer, J., Bulirsch, R., Eds.; Springer: New York, NY, 1980, pp 244–313, DOI: 10.1007/978-1-4757-5592-3_5.

(67) Busnengo, H. F.; Salin, A.; Dong, W. Representation of the 6D Potential Energy Surface for a Diatomic Molecule near a Solid Surface. *J. Chem. Phys.* **2000**, *112*, 7641–7651, DOI: 10.1063/1.481377.

(68) Verlet, L. Computer "Experiments" on Classical Fluids. I. Thermodynamical Properties of Lennard-Jones Molecules. *Phys. Rev.* **1967**, *159*, 98–103, DOI: 10.1103/PhysRev.159.98.

(69) Behler, J.; Parrinello, M. Generalized Neural-Network Representation of High-Dimensional Potential-Energy Surfaces. *Phys. Rev. Lett.* **2007**, *98*, 146401, DOI: 10.1103/PhysRevLett.98.146401.

(70) Plimpton, S. Fast Parallel Algorithms for Short-Range Molecular Dynamics. *J. Comput. Phys.* **1995**, *117*, 1–19, DOI: 10.1006/jcph.1995.1039.

(71) Singraber, A.; Behler, J.; Dellago, C. Library-Based LAMMPS Implementation of High-Dimensional Neural Network Potentials. *J. Chem. Theory Comput.* **2019**, *15*, 1827–1840, DOI: 10.1021/acs.jctc.8b00770.

(72) Deuflhard, P. Order and Stepsize Control in Extrapolation Methods. *Numer. Math.* **1983**, *41*, 399–422, DOI: 10.1007/BF01418332.

(73) Deuflhard, P. Recent Progress in Extrapolation Methods for Ordinary Differential Equations. *SIAM Rev.* **1985**, *27*, 505–535, DOI: 10.1137/1027140.

(74) Jackson, B.; Nattino, F.; Kroes, G.-J. Dissociative Chemisorption of Methane on Metal Surfaces: Tests of Dynamical Assumptions Using Quantum Models and Ab Initio Molecular Dynamics. *J. Chem. Phys.* **2014**, *141*, 054102, DOI: 10.1063/1.4891327.

(75) Liu, Q.; Zhang, L.; Li, Y.; Jiang, B. Ring Polymer Molecular Dynamics in Gas–Surface Reactions: Inclusion of Quantum Effects Made Simple. *J. Phys. Chem. Lett.* **2019**, *10*, 7475–7481, DOI: 10.1021/acs.jpclett.9b02570.

(76) Rodríguez-Fernández, A.; Bonnet, L.; Crespos, C.; Larrégaray, P.; Díez Muiño, R. When Classical Trajectories Get to Quantum Accuracy: The Scattering of H_2 on Pd(111). *J. Phys. Chem. Lett.* **2019**, *10*, 7629–7635, DOI: 10.1021/acs.jpclett.9b02742.

(77) Ghassemi, E. N.; Smeets, E. W. F.; Somers, M. F.; Kroes, G.-J.; Groot, I. M. N.; Juurlink, L. B. F.; Füchsel, G. Transferability of the Specific Reaction Parameter Density Functional for H_2 + Pt(111) to H_2 + Pt(211). *J. Phys. Chem. C* **2019**, *123*, 2973–2986, DOI: 10.1021/acs.jpcc.8b11018.

(78) Kroes, G.-J. Six-Dimensional Quantum Dynamics of Dissociative Chemisorption of H_2 on Metal Surfaces. *Prog. Surf. Sci.* **1999**, *60*, 1–85, DOI: 10.1016/S0079-6816(99)00006-4.

(79) Kroes, G.-J.; Somers, M. F. Six-Dimensional Dynamics of Dissociative Chemisorption of H_2 on Metal Surfaces. *J. Theor. Comput. Chem.* **2005**, *04*, 493–581, DOI: 10.1142/S0219633605001647.

(80) Craig, I. R.; Manolopoulos, D. E. Quantum Statistics and Classical Mechanics: Real Time Correlation Functions from Ring Polymer Molecular Dynamics. *J. Chem. Phys.* **2004**, *121*, 3368–3373, DOI: 10.1063/1.1777575.

(81) Habershon, S.; Manolopoulos, D. E.; Markland, T. E.; Miller, T. F. Ring-Polymer Molecular Dynamics: Quantum Effects in Chemical Dynamics from Classical Trajectories in an Extended Phase Space. *Annu. Rev. Phys. Chem.* **2013**, *64*, 387–413, DOI: 10.1146/annurev-physchem-040412-110122.

(82) Behler, J. Atom-Centered Symmetry Functions for Constructing High-Dimensional Neural Network Potentials. *J. Chem. Phys.* **2011**, *134*, 074106, DOI: 10.1063/1.3553717.

(83) Behler, J. Representing Potential Energy Surfaces by High-Dimensional Neural Network Potentials. *J. Phys.: Condens. Matter* **2014**, *26*, 183001, DOI: 10.1088/0953-8984/26/18/183001.

(84) Shakouri, K.; Behler, J.; Meyer, J.; Kroes, G.-J. Accurate Neural Network Description of Surface Phonons in Reactive Gas–Surface Dynamics: N_2 + Ru(0001). *J. Phys. Chem. Lett.* **2017**, *8*, 2131–2136, DOI: 10.1021/acs.jpclett.7b00784.

(85) Shakouri, K.; Behler, J.; Meyer, J.; Kroes, G.-J. Analysis of Energy Dissipation Channels in a Benchmark System of Activated Dissociation: N_2 on Ru(0001). *J. Phys. Chem. C* **2018**, *122*, 23470–23480, DOI: 10.1021/acs.jpcc.8b06729.

(86) Nattino, F.; Díaz, C.; Jackson, B.; Kroes, G.-J. Effect of Surface Motion on the Rotational Quadrupole Alignment Parameter of D_2 Reacting on Cu(111). *Phys. Rev. Lett.* **2012**, *108*, 236104, DOI: 10.1103/PhysRevLett.108.236104.

(87) Mondal, A.; Wijzenbroek, M.; Bonfanti, M.; Díaz, C.; Kroes, G.-J. Thermal Lattice Expansion Effect on Reactive Scattering of H_2 from Cu(111) at T_s = 925 K. *J. Phys. Chem. A* **2013**, *117*, 8770–8781, DOI: 10.1021/jp4042183.

(88) Brink, D.; Satchler, G., *Angular Momentum*, 2nd ed.; Oxford University Press: 1968; 87 pp.

(89) Auerbach, D. J. In *Atomic and Molecular Beam Methods*, Scoles, G., Ed.; Oxford University Press: 1988; Vol. 1, pp 362–379.

(90) Michelsen, H. A.; Auerbach, D. J. A Critical Examination of Data on the Dissociative Adsorption and Associative Desorption of Hydrogen at Copper Surfaces. *J. Chem. Phys.* **1991**, *94*, 7502–7520, DOI: 10.1063/1.460182.

(91) Louis, T. A. Confidence Intervals for a Binomial Parameter after Observing No Successes. *Am. Stat.* **1981**, *35*, 154–154, DOI: 10.1080/00031305.1981.10479337.

(92) Baule, B. Theoretische Behandlung Der Erscheinungen in Verdünnten Gasen. *Ann. Phys.* **1914**, *349*, 145–176, DOI: 10.1002/andp.19143490908.

(93) Goodman, F. O.; Wachman, H. Y. *Formula for Thermal Accommodation Coefficient*; 66-1; Cambridge, Massachusetts: M.I.T. Fluid Dynamics Research, 1966, DOI: 10.21236/ad0631007.